



Microgravity effect of inter-seismic crustal dilatation

Hojjat Kabirzadeh ¹✉, Jeong Woo Kim¹, Arezou Hadi Najafabadi², Joe Henton³, Ricky Kao ¹ & Michael G. Sideris¹

Changes in the density of the shallow crust has been previously related to co-seismic strain release during earthquakes, however, the influence of inter-seismic deformation on crustal density variations is poorly understood. Here we present gravity observations from the iGrav superconducting gravimeter in southern Vancouver Island, British Columbia, Canada which reveal a substantial gravity increase between July 2012 and April 2015. We identify a negative correlation between this gravity increase and crustal dilatation strain derived from horizontal GPS velocities. The overall increasing gravity trend is caused by the gravity increase during and immediately before and after episodic tremor and slip events, which is partially compensated by gravity decrease occurring between the events. We conclude that the observed gravity increase results from a density increase due to crustal compression and that this is mostly a result of inter-seismic strain accumulation during the subduction of the Juan de Fuca plate beneath the North American plate.

¹Department of Geomatics Engineering, University of Calgary, Calgary, AB T2N 1N4, Canada. ²Department of Geophysics, International Institute of Earthquake Engineering and Seismology, Tehran, Iran. ³Natural Resources Canada, Pacific Geoscience Centre, Sidney, BC V8L 4B2, Canada.
✉email: hkabrza@ucalgary.ca

Mass redistribution due to crustal deformation can cause variations in the gravity field. Gravimetric methods can detect the co-seismic, inter-seismic, and post-seismic effects of deformation. Numerous studies have focused on monitoring the co-seismic¹ or post-seismic² deformations due to earthquakes by utilizing Global Positioning System (GPS) data with Gravity Recovery and Climate Experiment (GRACE) monthly gravity solutions. The dislocation theory developed by Sun and Okubo³ demonstrated that the GRACE satellite can detect mass redistributions caused by earthquakes with magnitudes of 7.5 or greater, such as the 2010 Mw = 8.8 Central Chile (Maule) earthquake⁴, the 2011 Mw = 9.0 Tohoku-Oki earthquake⁵, and the 2012 Mw = 8.6 Wharton basin earthquake off-Sumatra⁶.

Recently, a few studies investigated the dilatation strain rates associated with earthquake mechanisms and confirmed their correlation with gravity observations. Dilatation strain is defined as a fractional decrease in area (horizontal dilatation), or volume (volumetric dilatation) caused by deformation. Additionally, a negative horizontal dilatation in crust is considered a crustal shortening while a negative volumetric dilatation strain in crust represents a crustal compression. Liangyu et al.⁷ studied the effect of the deformation of a density gradient zone and calculated the contribution of dilatation on gravity. Eshagh et al.⁸ implemented a theoretical model to estimate the stress-strain redistribution caused by the Sar-e-Pol Zahab 2018 earthquake in Iran by using the GRACE Follow-On (GFO) monthly solutions. Yin and Xu⁹ proposed a methodology to model the gravity effect of dilatation strain and found a negative linear correlation between changes in gravity and horizontal dilatation strain over the Tibetan Plateau that is equivalent to a crustal shortening. Their model showed that most crustal parts of the Tibetan Plateau are undergoing extension, which generates negative gravity signals at a rate of approximately 0.2 $\mu\text{Gal year}^{-1}$. Their results are confirmed by numerical modelling of the crustal tectonics in the Taiwanese Orogen^{10,11} and suggested a mass accumulation process beneath the crust of the northern Tibetan Plateau.

The Cascadia Subduction Zone (CSZ) in the northeast Pacific is the area with a long subducting fault where the Juan de Fuca Plate is diving beneath the North American plate¹² at a mean horizontal velocity of 40 mm year⁻¹. According to the fault's change of frictional properties with depth, the CSZ can be separated into a locked zone, a transition zone, and a slip zone (Fig. 1). The width of the locked zone is 60 km to 100 km with 10° dipping thrust, and the following down-dip transition zone is 60 km wide before the full rupture of slip zone^{13–15}. The accumulative energy is stored in the locked zone of CSZ, and eventually the strain is released, which results in megathrust earthquakes at intervals ranging from 500 to 600 years^{16,17}. The latest megathrust earthquake in CSZ was a M9.0 earthquake on January 26, 1700, and the recurrence probability of such a large earthquake in the next 50 years has risen from 10% to 37%¹⁸. Other than megathrust earthquakes, the processes of tectonic movement in CSZ are subduction, inter-seismic uplift, accretion, postglacial rebound, active volcanism, and Episodic Tremor and Slip (ETS)^{19–22}.

ETS, also known as silent earthquake, is a weak seismic event which releases energy over a period of hours to months, rather than a typical earthquake with a characteristic period of seconds to minutes. ETS is regarded as a foreshadowing of megathrust earthquakes that have been found in many subduction zones^{23–27}. In recent years, geophysical methods for ETS monitoring in western Canada have used arrays of broadband seismometers, borehole strainmeters (BSMs), tiltmeters, and GPS receivers^{28,29}. In addition to these methods, gravimetric methods can be used to illustrate the mass transfer of inter-seismic deformation and ETS events. The release of water content from the subducted young, hot, and wet oceanic crust generates a supercritical fluid at the plate interface. In

addition, metamorphic dehydration and partial melting are prominent during the subduction of oceanic crustal rocks to forearc depths²³. Nonetheless, the mass movement of magmatic or hydrothermal fluids can lead to subtle surface gravity changes. The detectable effects of inter-seismic deformation on gravity signal include both the vertical ground displacement and the density change due to dilatation strain.

Permanent strain accumulation is caused by both elastic interactions between crustal blocks and inelastic deformation associated with the megathrust earthquake cycle on the underlying subduction zone³⁰. At a recurrent interval of 13–16 months, an ETS event occurs by a slow slip in the deeper (25–45 km) part of northern CSZ accompanied by seismic tremor in 1–5 Hz frequency band^{24,31}. While some investigations demonstrated that the rate of strain release during major ETS events accounts for almost half the accumulated strain in each cycle and smaller ETS events are responsible for the rest of the strain release, some other numerical models suggest that a significant portion (~30–50%) of the slip deficit remains uncompensated after several events³². It is worth mentioning that a secondary locking procedure may be present at and beyond the ETS zone near the intersection of the Moho of the North American plate with the subducting plate interface because of fluid migration from the dehydrating slab, a change in frictional stability or temperature, or a change in bulk strength of materials³². As a result, the rupture of the next mega earthquake may be extended to the ETS zone which is located near large population cities.

For the investigation of ETS, the most useful measurements are continuous GPS station movements. There are numerous GPS sites located in northwestern United States and southwestern British Columbia^{33,34} that have been established and provided by the Natural Resources Canada (NRCAN) and the U.S. Geological Survey (USGS). Figure 1b shows the horizontal (arrow direction) and vertical (color map) velocities at 38 GPS sites in this region. A band of vertical change runs from QUAD (north) to P400 (south) in upward trend, and from P441 (north) to KTBW (south) in downward trend. The PGC site is located at the edge of the slip zone with minimal vertical movement.

A few studies used an FG5 absolute gravimeter and GPS measurements on Vancouver Island to detect ETS and their likely mechanisms. Lambert et al.³⁵ found inter-annual variations of gravity at 11 North American absolute gravity sites with a period of 6.85 years and concluded that this gravity change is most likely caused by mass redistribution without vertical displacement. Their fitted ETS model also revealed seven events and a common inter-slip recovery rate from 1997 to 2003. Mazzotti et al.³⁶ showed that the ETS events are always induced by mass redistributions of tectonic origin. They discovered an unexplained 0.53 $\mu\text{Gal year}^{-1}$ average rate of gravity change (positive direction of gravity is downward) at five sites in southwestern British Columbia and estimated a mean gravity to upward displacement ratio of $-0.24 \mu\text{Gal mm}^{-1}$ in this region. Nonetheless, the estimated gravity to upward displacement ratio may contain large uncertainties^{35,37}. A long-period mass increase from an unknown near-surface or deep-seated source was suggested in their study as a possible cause of the absolute gravity bias. Despite efforts made in these studies, the gravity signature of the inter-seismic crustal dilatation and ETS events in western Canada remains unknown.

In this study, the relationship between gravity changes and dilatation strain rates in the CSZ is explored. As GRACE satellite monthly solutions suffer from correlated errors and like absolute gravity campaigns do not provide high-frequency changes in gravity, we use the GWR Instruments Inc.'s iGrav[®] superconducting gravimeter (SG), which can provide 1-Hz gravity signals for years continuously. Further, it provides unprecedented sub- μGal precision³⁸ (1 nanoGal in the frequency domain and

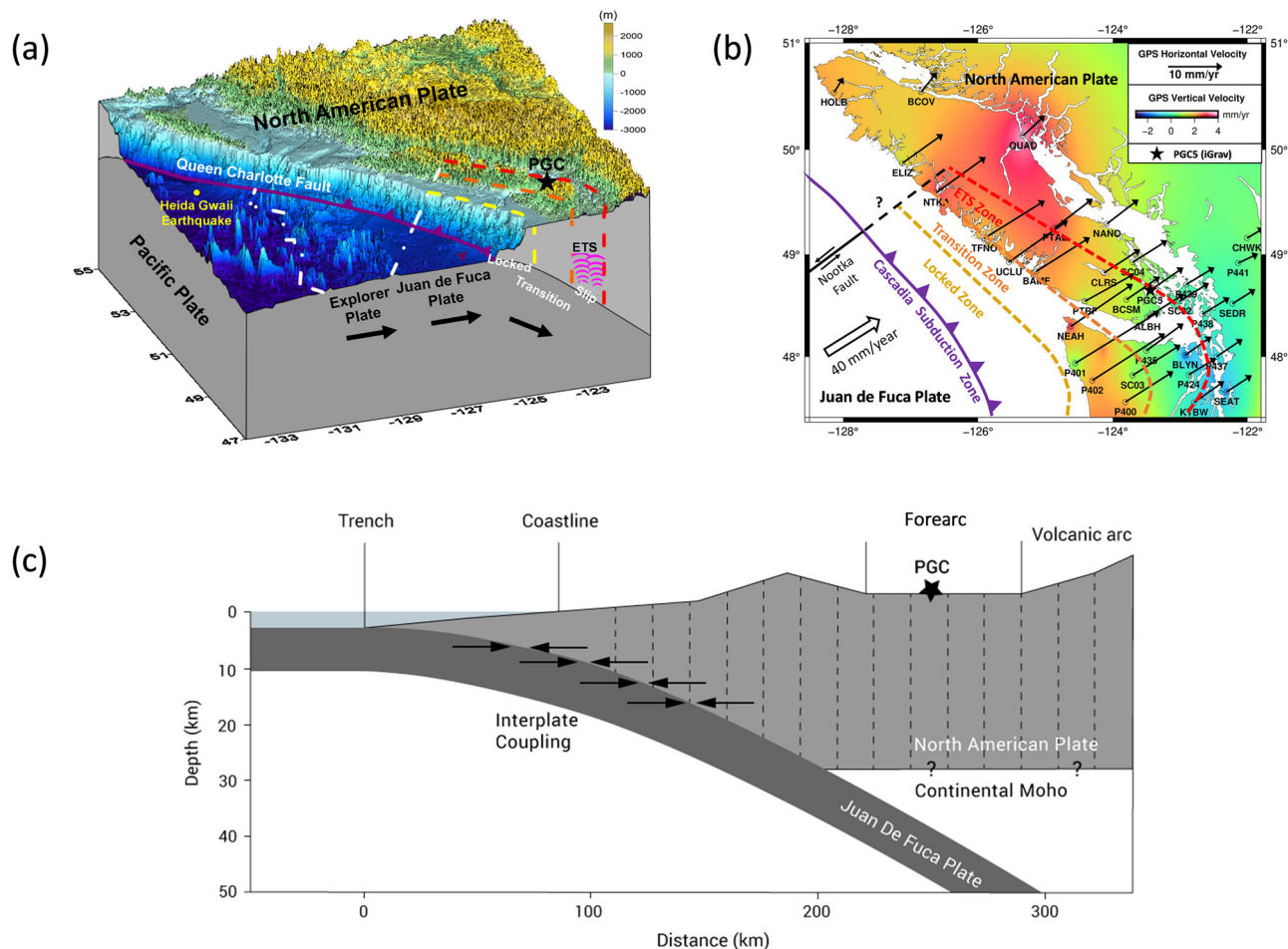


Fig. 1 Map and schematic view of the Cascadia subduction zone. **a** Topography and locations of the epicenter of the Haida Gwaii earthquake and the iGrav® SG at PGC; **(b)** Velocities of the horizontal crust movement (arrow direction) and vertical crust movement (color map) interpolated from 38 GPS sites along with the surface projection of locked, transition and ETS zones¹³. The map was created by using the Generic Mapping Tools (GMT)⁷¹; **(c)** Schematic cross section view of the CSZ and the location of PGC. The prisms used for gravity modelling are shown with dashed lines.

0.05 μGal in the time domain for 1 minute average) with very low drift of less than $0.5 \mu\text{Gal month}^{-1}$. After reduction of all known environmental effects, this study investigates the relationship between gravity changes and mass changes caused by tectonic deformations in western Canada. Accordingly, GPS observations in a network around northwestern United States and southwestern British Columbia are used to determine the inter-seismic dilatation strain. The density change associated with the dilatation strain is then used to calculate a theoretical strain-related gravity and the results are compared to the SG’s observations. Finally, the impact of earthquakes and ETS events on the gravity signal is investigated in detail.

Results

To reveal the gravity changes associated with earthquakes and ETS in CSZ, we deployed the iGrav® SG (serial number 001) at Pacific Geoscience Centre (PGC) in July 2012. During the observations, the nearest and largest shock detected by the iGrav was the Haida Gwaii earthquake (52.788°N , 132.101°W) with magnitude 7.8, which occurred at 03:04:08 UTC on October 28th, 2012, in the 14-km depth of Queen Charlotte Fault (QCF) (Fig. 1a). The rupture of post-shock was extended approximately 200-250 km along QCF while the distance between QCF and PGC was 760 kilometers.

The residual gravity of the SG after reduction of the environmental effects (Gravity data processing, methods) is illustrated in

Fig. 2a with a clear increasing trend rate. The gravity signal contains a few steps occurring on October 28th 2012, and August 21st and 22nd 2013. We detected two major events on these two dates. One of the events is associated with two large offsets, with a total of $\sim 3.4 \mu\text{Gal}$ gravity increase in two consecutive days of August 21st and 22nd, 2013. This coincides with a two-day event when the iGrav’s coldhead was replaced due to a required maintenance. Treating the $3.4 \mu\text{Gal}$ step due to the maintenance event in the gravity signal results in a total gravity trend of $\sim 1.8 \mu\text{Gal}$ or, equivalently, $\sim 0.65 \mu\text{Gal year}^{-1}$ as shown in Fig. 2c. The uncertainty of the residual gravity after reduction of environmental noise is estimated to be $0.5 \mu\text{Gal}$ ^{39,40}.

The other event that corresponds with a $-2.6 \mu\text{Gal}$ gravity change coincides with the Haida Gwaii earthquake that occurred on October 28th 2012 (Supplementary Fig. 1). There is no permanent offset observed in the BSMs, or other hydrological sensors in the vicinity of the PGC station which coincides with the earthquake and can be considered as evidence of a mass change. In addition, there is a large distance of $\sim 760 \text{ km}$ between QCF and PGC which makes it difficult to connect the earthquake-related fault dislocations to this gravity change. Intense earthquakes imposed on the SGs cause dislocation of the sensor from the equilibrium position and generate disturbances in the superconducting magnetic field of the SG. Some of these disturbances in the magnetic field are permanent and create permanent large offsets in gravity measurements, while others are gradually recovered

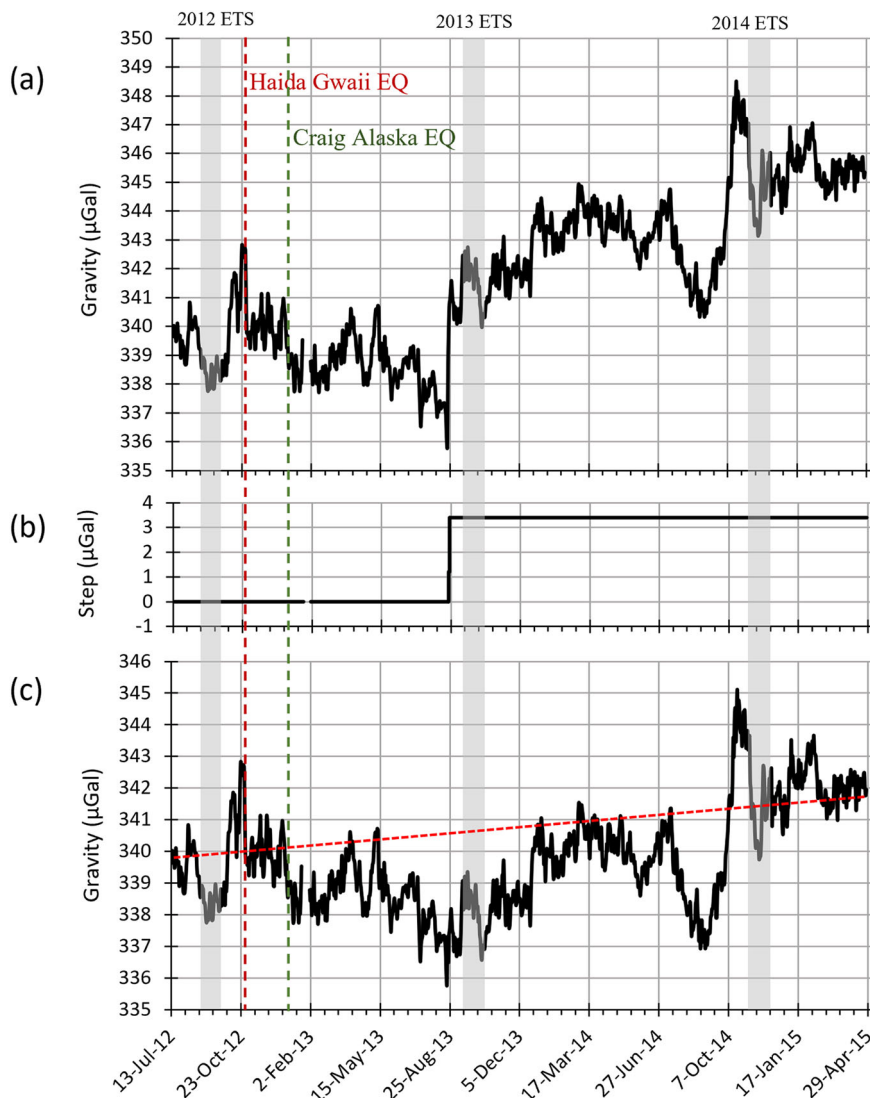


Fig. 2 Residual gravity signal after reduction of environmental effects. **a** Residual gravity of the SG after correction of tides, polar motion, atmospheric pressure, and soil moisture effects, before step correction; **(b)** Step function; **(c)** Residual gravity after correction of August 21st and 22nd, 2013 steps. The gray time-period columns represent ETS events at CSZ.

as the magnetic field stabilizes. Although there is a lack of strong evidence regarding a real mass change around the PGC at present, this co-seismic gravity change is not considered as an artifact and therefore remains in the gravity signal.

It is worth mentioning that another earthquake known as Craig Alaska earthquake (55.393°N , 134.652°W) occurred on January 5th 2013 at 08:58:19 UTC with magnitude 7.5 at a depth of 10 km. While some co-seismic disturbances were observed in the gravity signal correspondingly, this earthquake occurred at a 1060 km distance from the PGC and did not cause a detectable offset in gravity observations.

Three major ETS events were distinguished from both tremor events and GPS data during the operation period of the SG at PGC. The daily number of tremor events (Fig. 3a) was obtained from more than 300 seismograph stations distributed across a region including northwestern Washington State and southwestern British Columbia provided by Pacific Northwest Seismic Network (PNSN). The northern, eastern, and vertical detrended displacement measurements, averaged from the PGC5 and BCNS GPS stations located at PGC, are also shown in Fig. 3. The first ETS event occurred between September 1st and September 23rd 2012, the second one was observed from September 14th to October 8th

2013, and the third one was recorded from November 3rd to November 26th 2014. The most prominent movements associated with these ETS events are recorded in the eastern GPS components. There are ~ 5 mm westerly movements during the 2012 and 2013 ETS events, and ~ 3 mm westerly movement during the 2014 ETS event. The GPS displacement trends during and beyond the ETS events suggest the existence of crustal deformation at CSZ.

Processed GPS velocities during the SG operation period were collected from 533 stations in the Pacific Northwest region, which includes southwestern Canada and northwestern United States, provided by Nevada Geodetic Laboratory (NGL)^{41,42}. We grouped the data in blocks with dimensions of 1.0° latitude and 0.8° longitude and assigned the median value to the median position (Fig. 4a). The major visible patterns in the velocity field include a clockwise rotation in the southern part resulted from a transition from North-Western to North-Eastern movement and a landward decrease in the magnitude of the velocities which indicates locking effect on the subduction zone. In the north, the velocities are mostly perpendicular to the contours of the top of subducted Juan De Fuca plate, which indicates dominance of the role of subduction in deformation especially in the southern Vancouver Island.

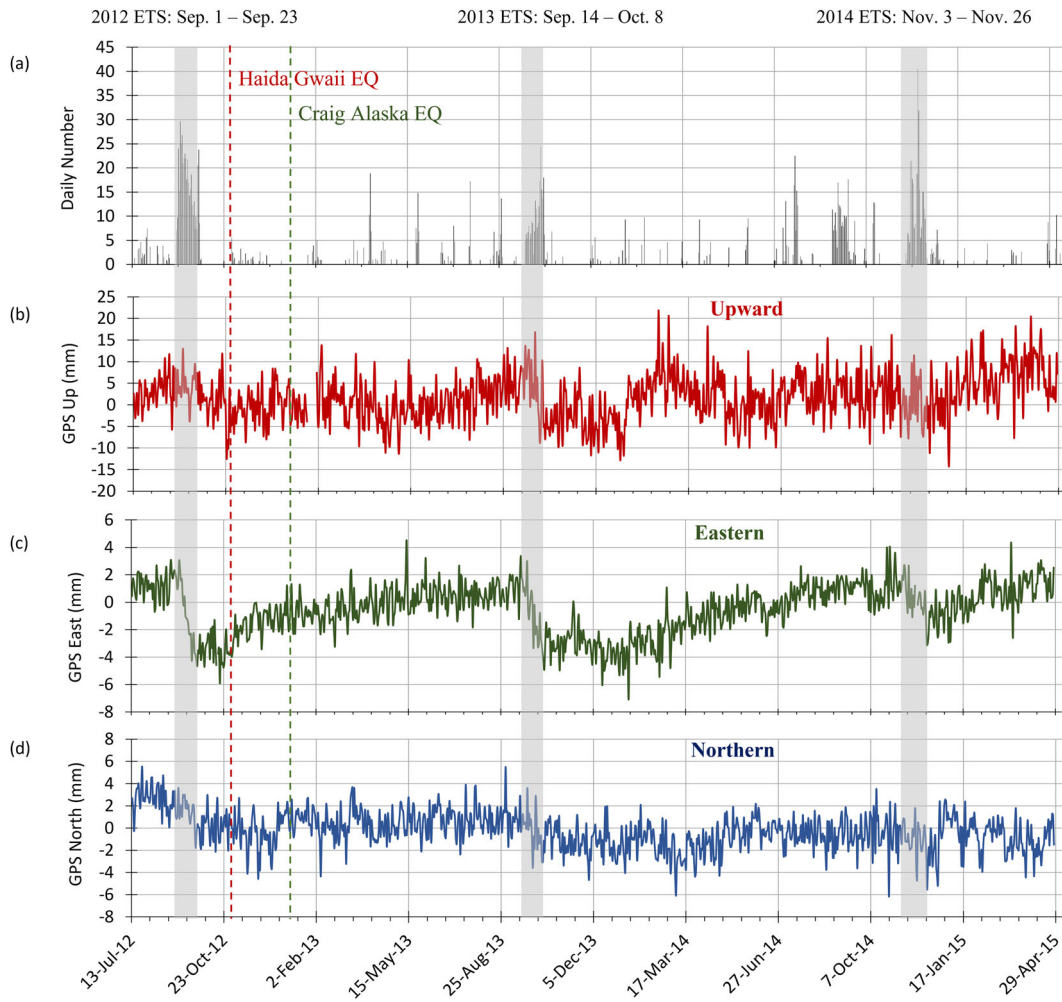


Fig. 3 Tremor and GPS observations at PGC. **a** Daily number of ETS events; **b**) Detrended upward movement; **c**) Detrended eastern movement; **d**) Detrended northern movement (PGC5 and BCNS stations). The gray time-period columns represent ETS events at CSZ.

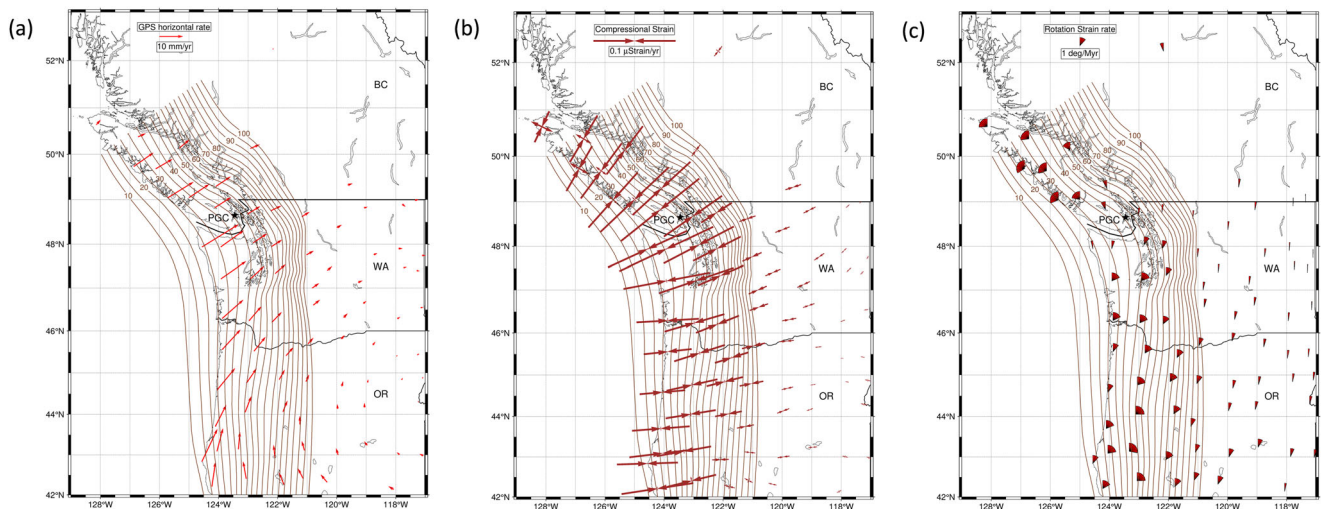


Fig. 4 GPS Velocity field and calculated strain components. **a** Horizontal velocity field, **b**) principal strain, and **c**) rotation rates from 533 stations in the Pacific Northwest region gridded in blocks with 1.0° latitude and 0.8° longitude dimensions. Contours show the Cascadia plate interface geometry based on the slab contours of McCrory et al.⁷². The maps were created by using the Generic Mapping Tools (GMT)⁷¹.

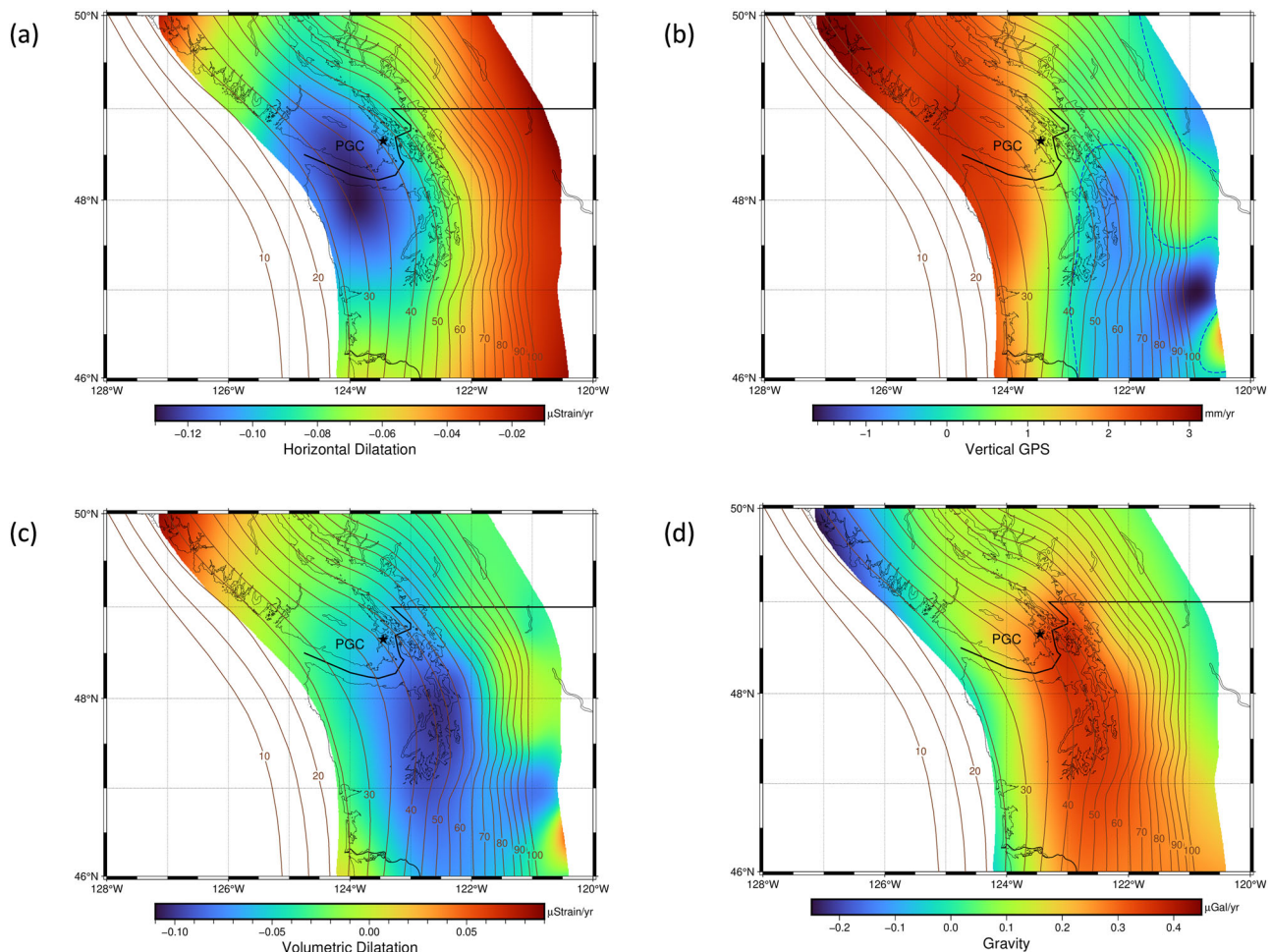


Fig. 5 Gravity effect of dilatation. **a** Horizontal dilatation strain, **(b)** vertical GPS velocity (Blue dashed curve represents zero vertical velocity), and **(c)** volumetric dilatation strain derived from GPS velocities in the Pacific Northwest region; **(d)** Gravity effect of volumetric dilatation strain. Contours show Cascadia plate interface geometry based on the slab contours of McCrory et al.⁷². The maps were created by using the Generic Mapping Tools (GMT)⁷¹.

The processed eastward and northward velocities were used to calculate deformation tensor using the least-squares collocation method included in the GeoStrain software⁴³. The resulted strain rates that are obtained from the symmetric part of the deformation tensor and rotation rates that are defined by the antisymmetric part of the deformation tensor are displayed in Fig. 4b c. We observe minimal rotation rates and the largest strain rates in the area around the PGC. In addition, the clockwise rotation of the southern block is replaced by a counterclockwise rotation to the north of the PGC.

The horizontal dilatation rates ($E_{ee} + E_{nn}$), calculated from the strain rates (Fig. 5a) show a maximum shortening rate of $0.13 \mu\text{Strain year}^{-1}$ southwest of the PGC and a $0.09 \mu\text{Strain year}^{-1}$ shortening rate calculated at PGC that is extended to a broader region with less magnitude. The high negative horizontal dilatation anomaly is located over the locked zone at which a large slip deficit rate has been observed⁴⁴. The results at the edges of the strain map are less accurate and we expect larger negative horizontal dilatations, specifically towards the Pacific Ocean⁴⁵. Furthermore, the accuracy of the calculated dilatation at the northern part suffers from both the edge effect and the sparsity of GPS stations. Our GPS-derived horizontal dilatation is also confirmed by Cruikshank and Peterson⁴⁶ who obtained a rough estimate of $\sim 0.1 \mu\text{Strain year}^{-1}$ for regional shortening from the GPS network in the north-western Washington State and southern Vancouver Island.

A reasonably accurate vertical strain (E_{zz}) is required to be added to horizontal dilatation ($E_{ee} + E_{nn}$) and form volumetric

dilatation ($E_{ee} + E_{nn} + E_{zz}$), which is used to calculate strain-related density and, subsequently, gravity change. Although vertical GPS velocities suffer from large uncertainties, the dense coverage of the Pacific Northwest GPS network makes it possible to estimate an acceptable regional vertical displacement, using the same procedure that was used for generating the horizontal velocity field (Fig. 5b). The vertical strain was then calculated for each block by dividing the vertical displacement to the depth of each block which is considered the depth to the Moho boundary or the top of the subducting plate and assuming a negligible Moho vertical displacement (Fig. 1c). By adding the vertical strain to the horizontal dilatation and calculating volumetric dilatation rates, a $\sim 0.07 \mu\text{Strain year}^{-1}$ compression was obtained at PGC (Fig. 5c). While the maximum shortening accumulation occurs at the regions with a depth to subducting plate of less than 45 km which coincides with the downdip end of the slip zone, the maximum compression occurs in the regions beyond the ETS zone, where we observe shortening (Fig. 5a) accompanied with ground subsidence (Fig. 5b).

To calculate the gravity effect of volumetric dilatation, the estimated dilatation rates were first interpolated at the center of the previously made blocks and, in the absence of information regarding the variation of the dilatation with depth, we assume a uniform dilatation in each block and a decoupled crust–mantle boundary. The depth of each block was fixed at the top of the subducting plate with a maximum depth of 45 km as the seismic

coupling depth which was inferred from seismic reflections^{47–49} and thermal models^{19,50}.

Figure 5d demonstrates the modelled gravity effects of the volumetric dilatation distribution by calculating and adding the gravity effect of each block using Eqs. (4) and (5) and considering a 2790 kg.m^{-3} crustal density. The crustal compression and subsequently gravity is reduced at areas with a large upward ground displacement trend towards the locked zone. Additionally, the downward ground displacement east of the PGC supports the crustal shortening and generates a larger gravity anomaly which is extended southward into western Washington State. The results indicate a maximum of $\sim 0.43 \mu\text{Gal year}^{-1}$ gravity change to the northwest of PGC while the gravity rate is $\sim 0.4 \mu\text{Gal year}^{-1}$ at the PGC location.

To investigate how the depth of effective strain can change the modelled gravity, we repeated the calculations for both 30 km and 55 km depths. The former case could represent a coupled Moho and the latter could consider accumulated strain in the subducting plate, as both the subducting and overriding plates can store strain³². We obtained a maximum of $\sim 0.47 \mu\text{Gal year}^{-1}$ gravity change by considering a 55 km depth and by assuming a shallower depth of 30 km for the effective stress, the maximum gravity reaches $\sim 0.37 \mu\text{Gal year}^{-1}$. This demonstrates the significant impact of the strain in the shallower depths on the gravity. The complete workflow for calculation of dilatation gravity from GPS velocities is demonstrated in Supplementary Fig. 2.

Discussion

The gravity signal recorded at PGC consists of two major patterns. The first pattern is an increasing trend which is attributed to the portion of the inter-seismic strain that is accumulated, and a second pattern that includes a rise of the gravity around the ETS events that is compensated in the time-periods between the ETS events (Fig. 2c). The overall trend of the gravity signal ($\sim 0.65 \mu\text{Gal year}^{-1}$) has a good agreement with the historical absolute gravity trends ($\sim 0.53 \mu\text{Gal year}^{-1}$) in CSZ^{35,37}. The absolute gravity trend has been calculated as the offset of the linear regression of the gravity and ground displacement among several stations³⁶, and therefore represents the regional variations of the gravity field.

While gravity is normally compared to vertical displacement, we found a meaningful negative correlation coefficient of ~ -0.9 between the detrended eastward GPS data averaged from PGC5 and BCNS stations (Fig. 6b), and the residual gravity signal (Fig. 6c). The westerly movement of GPS at and around the ETS events is accompanied by a rise in gravity signal. However, a large portion of this gravity increase recedes after each event resulting in a smaller overall increasing gravity trend. The 2012 and 2013 ETS events begin with a westerly movement in GPS data and a minimal gravity increase which turns into a slower westerly movement accompanied with a quicker gravity increase after these events. For the time periods between the ETS events, we observe a gradual gravity decrease accompanied with easterly movement in GPS data.

The gravity increase corresponding to the 2014 ETS event is significant ($\sim 5 \mu\text{Gal}$) but in contrast to the other ETS events begins a few weeks before the main ETS event from the end of another period with high tremor activities occurring between September 1st and September 12th, 2014 (orange time-period in Fig. 6). In this minor event, a sharp westerly movement in GPS data is not observed and gravity signal remains unchanged. Another notable feature is also observed during 2014 main ETS event in which detrended easterly movement recedes half ($\sim 3 \text{ mm}$) the amount of westerly movement during 2012 and 2013 ETS events ($\sim 6 \text{ mm}$). It is worth mentioning that the gravity change is specifically

significant during the 2014 main event which includes a $\sim 4 \mu\text{Gal}$ drop during the main ETS event and is completely recovered by the end of the event. This behaviour is not observed during the other ETS events. The geographical and temporal distribution of the tremors during the three main ETS events are shown in Fig. 7. While tremors occur over a large area in Northwest-Southeast and the opposite directions during the 2012 and 2013 events (Fig. 7a b), negligible tremor events are observed during the 2014 event in a large area around PGC and southern Vancouver Island (Fig. 7c). In addition, during the suspicious second 2014 tremor event (Fig. 7d), the tremor activities occur in the vicinity of the PGC location which can be evidence of a minor slip and can explain the timing of the rise in gravity signal before the main 2014 ETS event.

To understand the source of the high frequency changes in the gravity signal, a more comprehensive approach is required to calculate strain changes from GPS movements in short time periods. Nonetheless, we used an intuitive approach and subtracted the eastern and northern movements of SC02 GPS station located 34 km east of the PGC from the eastern and northern movements of the BCSM station located 28 km west of the PGC (Fig. 1b) and compared the results with the residual gravity signal (Fig. 6d e). The relative movement in the direction of subduction at CSZ is also calculated and displayed in Fig. 6f. The azimuth angle of the subduction is considered $\sim 145^\circ$ as an average of the plate movement direction around PGC. Although these movement differences are not representative of real strain changes, they can deliver a rough picture of directional dilatation strain between the two stations. In contrast to the Easterly movement at the PGC5 and BCNS GPS stations, the relative movements increase during and around all three ETS events which represents a compression during these events and supports the gravity increase.

Another interesting feature of the iGrav's gravity signal is the coincidence of the Haida Gwaii Earthquake occurrence with the timing of the 2012 ETS peak in the gravity signal, although this earthquake occurred $\sim 760 \text{ km}$ away from the iGrav's location. A more detailed investigation in future studies is necessary to find a possible link between the two events. It is worth mentioning that the megathrust earthquakes in CSZ are expected to have similar timing because during ETS events the accumulating elastic energy is released over the slip zone and some of compressional stress is transferred to the locked zone of the plate boundary resulting in an increased chance of the fault unlocking and rupture.

Conclusions

The impact of the strain in Cascadia Subduction Zone (CSZ) on gravity is investigated by continuous observations of an iGrav® superconducting gravimeter installed at the Pacific Geoscience Center (PGC) on Vancouver Island in British Columbia, Canada. After reduction of all known environmental gravity effects, the residual gravity signal demonstrates $\sim 1.8 \mu\text{Gal}$ increase ($\sim 0.65 \pm 0.38 \mu\text{Gal year}^{-1}$) from July 2012 to April 2015, which can be explained by mass redistribution. This increase is in good agreement with observed inter-annual increase of gravity ($0.53 \mu\text{Gal year}^{-1}$) at several North American absolute gravity sites in the past³⁵, which were not explained with vertical displacement. However, our estimated rate of iGrav's gravity change is considered a local effect which is larger than the estimated absolute gravity representing the regional effect.

Negative volumetric dilatation strain that represents a crustal compression can generate measurable gravity effects by increasing the density of the crust. This density change, although small, results in a considerable mass redistribution when it affects areas with hundreds of kilometers horizontal extension and tens of kilometers depth. We estimated a $\sim 0.09 \mu\text{strain year}^{-1}$ crustal shortening rate and a $\sim 0.07 \mu\text{strain year}^{-1}$ crustal compression rate at PGC derived

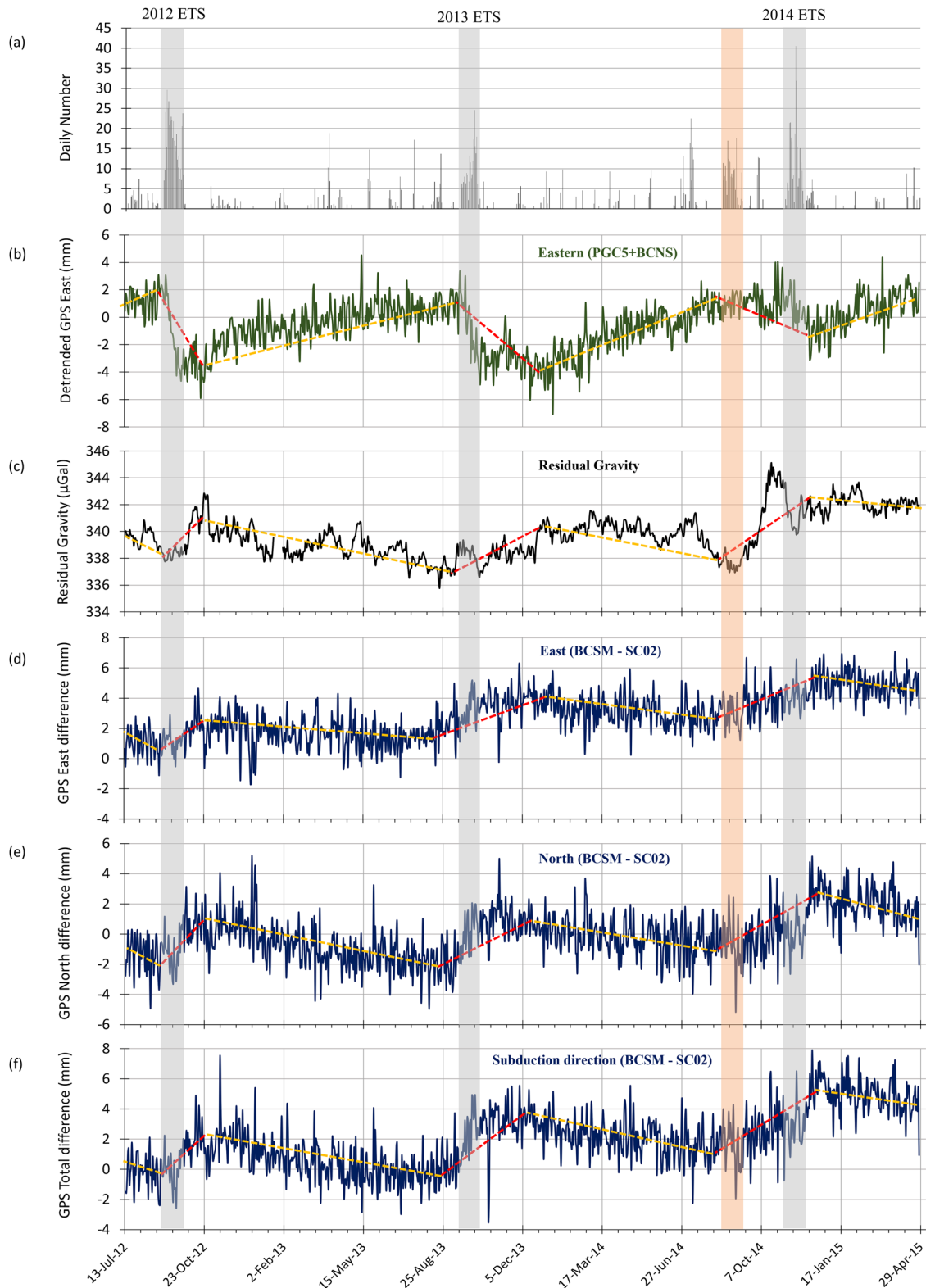


Fig. 6 Comparison of residual gravity with relative movement of GPS stations. **a** Daily number of ETS events; **(b)** Detrended eastern movement with red dashed lines indicating periods with westerly GPS trends and yellow dashed lines displaying periods with easterly GPS trends; and **(c)** Residual gravity with red dashed lines indicating periods with increasing gravity and yellow dashed lines displaying periods with decreasing gravity trends; **(d)** Relative eastern and **(e)** relative northern movement of BCSM GPS station with respect to SC02 station; **(f)** Relative movement of BCSM GPS station with respect to SC02 station in the direction of subduction. The three main ETS events occur in the gray time-period columns and a fourth period with high tremor activity is detected and shown with an orange column.

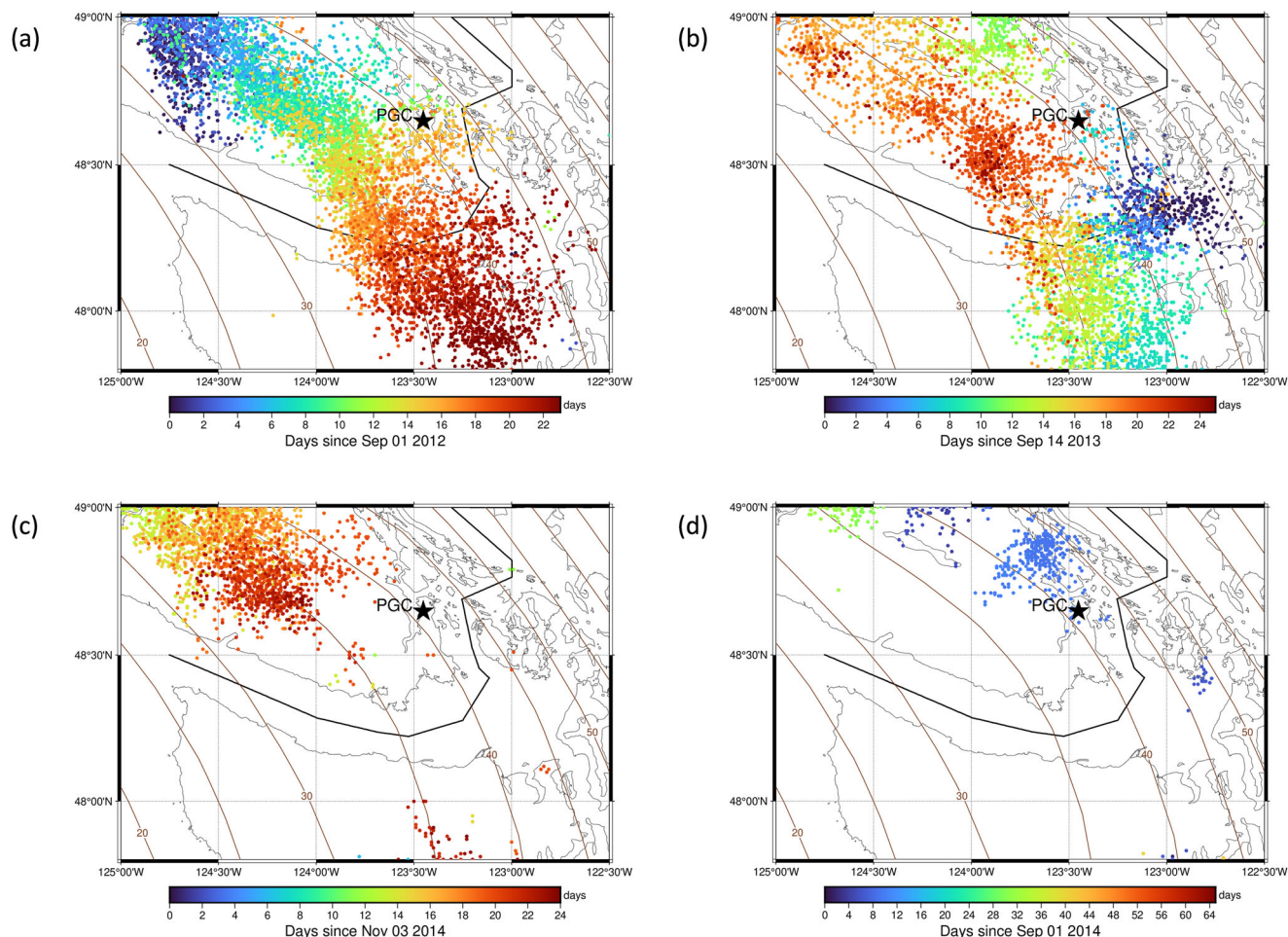


Fig. 7 Temporal and spatial distribution of ETS events. Location and timing of tremor during (a) 2012 main ETS event, (b) 2013 main ETS event, (c) 2014 main ETS event, and (d) the 2014 minor ETS event. Contours show Cascadia plate interface geometry based on the slab contours of McCrory et al.⁷². The maps were created by using the Generic Mapping Tools (GMT)⁷¹.

from GPS observations. Gravity forward modelling predicts $\sim 0.4 \pm 0.26 \mu\text{Gal}$ gravity increase due to the compression in a maximum depth of 45 km. An annual $\sim 0.65 \mu\text{Gal}$ gravity change detected from SG observations requires the shortening to be effective in a larger depth. A part of this extra depth may be explained by mass accumulation from the subducted Juan De Fuca plate as strain can be accumulated on both plates. Considering the sub- μGal level accuracy of the residual gravity, a significant part of the residual gravity of $\sim 0.65 \mu\text{Gal year}^{-1}$ can therefore be explained by the theoretical deformation model.

The gravity signature of ETS related deformation was also investigated by comparing the gravity signal with the East-West GPS displacement. A clear inverse correlation between the two signals demonstrates a rise in gravity during and around the ETS events and a smaller gravity trend reversal between the events resulting in a net increase in the gravity over the PGC.

As gravity signal records high temporal resolution signature of density change due to accumulated strain, it can be used to track both the short-term and the permanent accumulated strain in CSZ. While a simple vertical displacement gravity correction is commonly applied to gravity measurements, this study recommends the dilatation strain correction in geophysical studies which focus on detection of subtle changes in the gravity field, as the effect can reach a μGal level inter-annual change in tectonically active regions. Installation of a permanent micro gravimeter at PGC can confirm the long-term gravity trend and reveal more details about the tectonic activities and earthquakes in western

Canada. Moreover, a better coverage of GPS network in western Canada can drastically improve our understanding about the complicated strain changes.

Methods

Gravity data processing. The iGrav SG was installed in October 2011 at the University of Calgary⁵¹. Portability and sensitivity tests were conducted over the next six months, where an accuracy of better than $1 \mu\text{Gal}$ was achieved after a successful reduction of environmental effects^{39,40}. The SG was deployed in July 2012 at the Natural Resources Canada (NRCan)'s PGC located on Vancouver Island near Sidney in British Columbia, Canada. PGC is located on the forearc of the northern CSZ and is equipped with FG-5 and A-10 absolute gravimeters, BSMs, a tide gauge, and a GPS station. The underground gravity vault at the PGC is covered by one meter thickness of soil. The iGrav was installed on a concrete platform in the vault, while the FG-5 and A-10 absolute gravimeters were installed on a measurement table in a large separate room next to the iGrav (Supplementary Fig. 3a).

One-second gravity measurements were recorded in the time period between July 14th 2012 and April 27th 2015 (Supplementary Fig. 4a). The calibration of the SG measurements was conducted by a regression between parallel observations of FG-5-106 absolute gravimeter and SG voltage recordings over the period from August 2nd to August 8th 2012 (Supplementary Fig. 3b). In this procedure, a 3 standard deviation (3σ) threshold was used to remove the outliers. A calibration factor of $-94.994 \mu\text{Gal volt}^{-1}$ was estimated and applied for obtaining the raw gravity signal. The relative precision of the calibration factor can approach 0.1%⁵² depending on the level of environmental and instrumental noise. The raw gravity signal was consequently resampled to 1-hour data using a low-pass least-squares filter. Additionally, the gravity signal contained a gap between January 20th 2013 and January 31st 2013 as a result of SG data acquisition system failure that was treated and filled with theoretical Earth tide gravity for data analysis procedures that need a continuous signal.

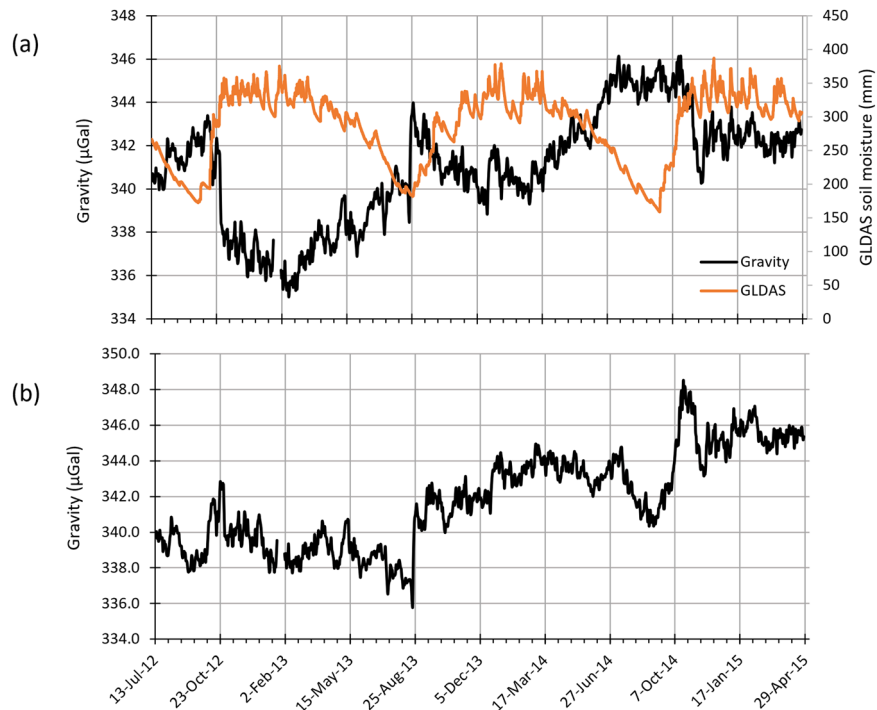


Fig. 8 Gravity correction of hydrological effects. a Residual iGrav gravity signal before hydrological correction (Black curve) and top 1 m soil moisture content from GLDAS models (Orange curve); **(b)** Hydrology corrected residual gravity.

Environmental interferences such as atmospheric pressure (g_{Atm}), hydrology (g_{Hyd}), ground vertical displacement (g_{Dis}), along with Earth tides (g_{Tide}), polar motion (g_{Pol}), and ocean loading (g_{Ol}) have the most significant influences on the SG recordings (g_{Obs}):

$$g_{Obs} = g_{Tide} + g_{Ol} + g_{Pol} + g_{Atm} + g_{Hyd} + g_{Dis} + g_{res}, \quad (1)$$

where g_{res} represents the residual gravity that includes the gravity effect of tectonic activities. The gravity effects of the solid Earth tide and ocean loading which dominate the SG's observations are calculated by the ETERNA program⁵³ which estimates tidal parameters by least-squares adjustment from the redundant observations. This process also considers periodic components of the ocean loading, hydrology and atmospheric pressure that have the same frequencies as the Earth tides⁴⁰. Supplementary Fig. 4d shows power spectral density (PSD) of the raw SG gravity signal versus that of the tide corrected signal which indicates effective reduction of periodic tide constituents from the gravity signal. At this stage, instrumental perturbations such as spikes were processed and reduced, however, steps in observations were unclear at this point and therefore were treated after reduction of all environmental effects. The polar motion effect on SG represents a long-periodic effect, and the dominant frequency is associated with the period of Chandler wobble (about 435 days). The gravity change caused by this motion is obtained from³⁹:

$$\Delta g_{Pol} = 1.164\omega^2 R \sin 2\phi (x_p \cos \lambda - y_p \sin \lambda) \times 10^8, \quad (2)$$

where Δg_{Pol} is the polar motion effect in μGal , R is the radius of the spherical Earth model, ω is the angular velocity, ϕ and λ are latitude and longitude, and x_p and y_p are polar motion coefficients in radian that are provided and updated by the International Earth Rotation Service (IERS). The calculated polar motion gravity effect at the PGC site is shown in Supplementary Fig. 4b. Atmospheric and oceanic masses also lead to polar motion at shorter periods (diurnal and semi-diurnal periods), but these gravity effects are too small to be considered in this study⁵⁴.

The SG has been equipped with atmospheric pressure sensors, which deliver a measure of the distribution of air mass at a local scale. There are gravity changes caused by both the direct Newtonian attraction of the air masses and the changes due to the load of the air mass changes⁴⁰. Warburton and Goodkind⁵⁵ demonstrated that the atmospheric gravity effect is frequency dependent. To calculate this effect on the gravity signal, we used a frequency-dependent atmospheric pressure admittance factor⁵⁶ which applies constant magnitudes of about $0.3 \mu\text{Gal hPa}^{-1}$ for the low-frequency band (less than 0.1 cpd) and $0.44 \mu\text{Gal hPa}^{-1}$ for the high-frequency band (higher than 2 cpd). A linearly increasing admittance factor between 0.3 and 0.44 was also used for the remaining frequency band in the middle (Supplementary Fig. 4c).

Hydrological effects on gravity signal are the most complicated interferences and have the largest contribution to the uncertainty of the residual gravity. While

there is a groundwater well within 1 km area of the SG location, the effect of groundwater level depends significantly on the geological settings such as porosity and the shape of the aquifers. A major part of this effect is corrected in other hydrological corrections because of its correlation with other hydrological effects. Among all hydrological processes, soil moisture content has the most significant effect. Nonetheless, direct soil moisture measurements were available only during the first 8 months of SG observations. An alternative measure of soil moisture content was derived from the Noah V2.7.1 model provided by Global Land Data Assimilation System (GLDAS). This 3-hourly sampled dataset is available in a 0.25-degree spatial resolution from 2000 to the present⁵⁷. The GLDAS soil moisture models have been widely used to identify the regional-scale groundwater components in the GRACE total water storage observations⁵¹. We calibrated the GLDAS soil moisture data with eight months of local measurements of soil moisture at PGC. This dataset has been collected by four soil moisture sensors at 25, 50, 75 and 100 cm depths right above the gravimeter. The calibrated GLDAS soil moisture can reproduce the local effects by using an admittance of $0.038 \mu\text{Gal}$ for 1 mm of equivalent water height change derived from a linear regression with residual gravity of the iGrav. This admittance factor is smaller than the $0.042 \mu\text{Gal mm}^{-1}$ obtained from the Bouguer slab model and previous studies^{58,59}. It is worth mentioning that as the SG had been installed below the surface level, the soil moisture effect must be added to the gravity signal as the accumulated water mass above the gravimeter attenuates the gravity signal. Deeper hydrological effects such as groundwater variations, however, act below the gravimeter and therefore cancel out a small part of the soil moisture effect. The GLDAS derived soil moisture representing variations of water content in the top 1 m of soil at PGC, and the SG's gravity signal before and after hydrological corrections are shown in Fig. 8.

The residual gravity at this stage still contains the effects of non-periodic oceanic variations along with vertical displacement and deformation. As the periodic effects of tides have been reduced from the gravity signal, reduction of all other effects should be performed after de-tiding of the signals. A linear regression of the residual gravity and vertical displacement can determine the coefficient factor representing the gravity signature of this effect. Lambert et al.³⁵ found a linear relationship between the absolute gravity rates and the averaged GPS vertical rates in the CSZ region with a slope of $-0.18 \pm 0.03 \mu\text{Gal mm}^{-1}$, which is consistent with the theoretical value of $-0.2 \mu\text{Gal mm}^{-1}$ ⁶⁰. The vertical GPS data from PGC5 and BCNS stations shown in Fig. 3b contain high frequency variations and can introduce extra error if used for correction of ground displacement. Instead, we used an inverse distance weighted average of vertical displacement among a few neighbor stations (PGC5, BCNS, BCSM, BCES, ALBH, SC02, and P439) which reduces the uncertainty in vertical displacement to ~ 2 mm. A $-0.2 \mu\text{Gal mm}^{-1}$ admittance factor was then applied to the resulted vertical displacement shown in Fig. 9b and was reduced from the gravity signal.

It is worth mentioning that the variations in the vertical surface displacement originate from both tectonics and non-tectonic processes which include hydrological and atmospheric effects along with their load effects. Heki and Arief⁶¹

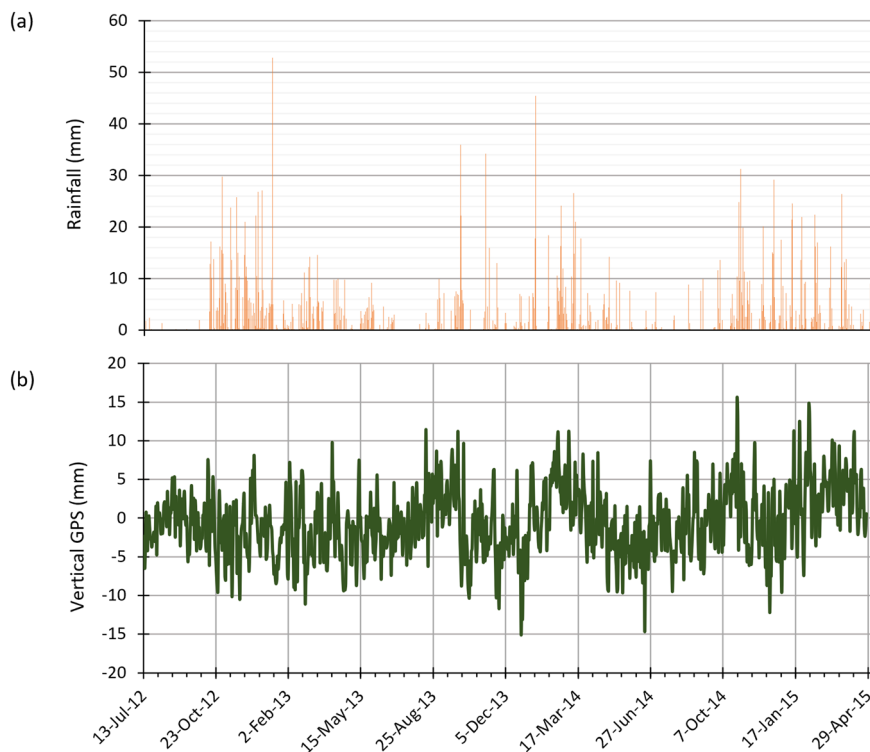


Fig. 9 Rainfall and vertical displacement at PGC. **a** Rainfall data collected from the weather station at Victoria airport located ~2 km away from PGC; **(b)** Vertical displacement at PGC obtained from an inverse distance weighted average of vertical displacement among a few stations around PGC (PGC5, BCNS, BCSM, BCES, ALBH, SC02, and P439).

investigated the influence of extreme weather, such as heavy rainfall and snowfall on crustal movement. They demonstrated that these events significantly change the water content of the soil layer and deform the crust up to 1-2 cm. Daily rainfall data collected from the weather station at Victoria airport located ~2 km away from PGC shown with orange bars in Fig. 9a indicates a subsidence after heavy rainfall events at PGC (Fig. 9b). Precipitation observations have been also used in composition of GLDAS models⁵⁷. Regression analysis between rainfall data and the hydrology-corrected gravity demonstrates negligible residual gravity effect of heavy rainfalls and confirms the estimated ~1 μGal uncertainty of the GLDAS models in previous studies⁶².

The direct attraction by local tidal waters has a small impact on the gravity observations as the gravimeter is almost located at the sea level. In addition, an accurate reduction of the ocean effect needs a complex model that considers phase changes as well. As the non-periodic effects of tide gauge data is also strongly connected to the atmospheric and hydrological processes³⁶, a major part of this effect could be removed in previous correction steps. The complete workflow for SG data processing is demonstrated in Supplementary Fig. 5.

Gravity modelling of dilatation. The effect of deformation on the gravity needs to be confirmed by theoretical modeling of the expected gravity signal from the shortening of the crust. The shortening can increase the density as more mass is concentrated in a constant volume. Although this density change may seem small, its gravity effect becomes considerable when it comes into effect in regions with a few hundreds of kilometers area and tens of kilometers depth. Han et al.⁶³ used GRACE observations to detect a ±15 μGal gravity change corresponding with the great December 2004 Sumatra-Andaman earthquake generated by roughly equal contributions of coseismic vertical displacement and density change of the crust and mantle due to volumetric dilatation. They used a dislocation model to estimate vertical displacement at the seafloor and Moho boundaries and calculated the associated volumetric dilatation, density, and gravity change. However, Cambiotti et al.⁶⁴ noted an overestimation of crustal dilatation calculated by Han et al.⁶³ and instead discovered a large local dilatation at the fault discontinuity and not in the whole crust. The gravitational effect of this dilatation is compensated by an opposite contribution from the crust uplift. After this localized dilatation is removed, Cambiotti et al.⁶⁴ predicted a compression in the footwall and dilatation in the hanging wall, which agrees with the seismic radiation pattern.

Yin and Xu⁹ developed a simple yet viable model to calculate the gravity effect of deformation using the Bouguer slab geometry. As the crust can be coupled to the mantle at the Moho boundary to some degree, the strain is not consistently distributed in depth and therefore a decoupling factor was introduced in their

gravity modelling. The gravity effect of a Bouguer slab is obtained from⁹:

$$\Delta g_b = -k\pi G\rho_c H_c (Eee + Enn), \tag{3}$$

where Δg_b is the gravity effect of a slab with H_c thickness and ρ_c density experiencing a horizontal dilatation strain of $Eee + Enn$ with negligible vertical strain, $G = 6.67384 \times 10^{-11} \text{ m}^3\text{kg}^{-1}\text{s}^{-2}$ is the gravitational constant, and $k = 2$ is the crust-mantle coupling factor for a completely decoupled Moho, while $k = 1$ corresponds to a completely coupled Moho⁹. Using this relationship for a decoupled crust with an average density of $2790 \text{ kg}\cdot\text{m}^{-3}$ and 45 km thickness, a gravity to horizontal dilatation ratio of $\sim -5.26 \text{ }\mu\text{Gal }\mu\text{strain}^{-1}$ is achieved. This ratio for a completely coupled crust-Moho boundary is half of the decoupled value. The Bouguer slab model is an acceptable approximation provided that the strain is not limited to a small area and the horizontal extension to thickness ratio remains large. Therefore, a more accurate gravity to strain ratio is slightly smaller than the Bouguer slab model. Moreover, this model ignores the effect of vertical deformation which is needed for calculating volumetric dilatation strain and density change.

We developed a more accurate model by considering the crust as a finite slab and modeled the gravity effect of volumetric dilatation within a rectangular prism with equal upper face sides (Sc). Plouff's relationship⁶⁵ is used to calculate the gravity effect at the center of the upper face of the prism⁶⁶⁻⁶⁹:

$$\Delta g_z(r) = -G\Delta\rho \sum_{p=1}^2 \sum_{q=1}^2 \sum_{s=1}^2 \mu_{pqs} \left[a_p \ln(b_q + \mu_{pqs}) + b_q \ln(a_p + \mu_{pqs}) - c_s \arctan\left(\frac{a_p b_q}{c_s r_{pqs}}\right) \right], \tag{4}$$

where, $\mu_{pqs} = (-1)^p(-1)^q(-1)^s$ with $p, q, s = \{1, 2\}$, $a_p = x_i - x'_p$, $b_q = y_i - y'_q$, $c_s = z_i - z'_s$, and $r_{pqs} = (a_p^2 + b_q^2 + c_s^2)^{1/2}$ is the distance between one corner of the prism located at (x'_p, y'_q, z'_s) and the observation point located at $r = (x, y, z)$. The density contrast in this equation is linearly dependent on the volume which is in turn determined by the volumetric dilatation of the crust:

$$\Delta\rho = -\rho_c(Eee + Enn + Ezz) \tag{5}$$

To determine if the gravity change because of dilatation is measurable and to obtain an estimation of the expected strength of the observed gravity, a feasibility test of the gravity effect of deformation is done by assuming a uniform 0.1 μstrain horizontal shortening (e.g., 10 mm in 100 km) and a negligible vertical strain (Ezz) in a prism with different horizontal dimensions (Sc) and thicknesses (Hc). As it is shown in Fig. 10, the gravity effect approaches a constant value as the horizontal dimension of the prism increases with respect to its thickness. The shortening in the CSZ is extended in hundreds of kilometers, from the northern parts of the Vancouver Island in Canada to the northwestern United States. By assuming a

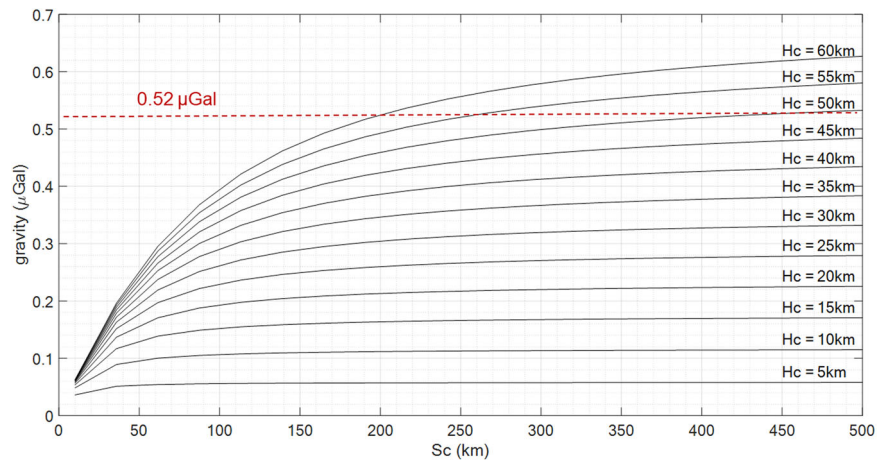


Fig. 10 Gravity forward modelling of dilatation strain. Gravity effect of 0.1 μ strain shortening in a prism with different vertical (H_c) and horizontal (Sc) dimensions.

shortening of 0.1 μ strain in an area covering 200 km by 200 km around PGC in each direction, a decoupled crust–mantle boundary and a strain concentrated in the top 60 km of the crust, a ~ 0.52 μ Gal gravity change is achieved.

Uncertainty analysis. The uncertainty in SG data processing include 1 μ Gal for the attraction and load effects of soil moisture and groundwater level, 0.05 μ Gal for atmospheric pressure, 0.1 μ Gal for non-tidal ocean circulation, 0.1 μ Gal for polar motion along with solid earth and ocean tides⁷⁰, 0.4 μ Gal for vertical displacement, and 0.05 μ Gal for observed superconducting gravity⁴⁰. As the uncertainty of hydrological correction is an order of magnitude larger than the uncertainty of other effects in the error propagation, 1 μ Gal is considered as the uncertainty of the SG residual gravity in this study⁴⁰. Further improvements in uncertainty of SG residual gravity can be obtained by deployment of local hydrological sources of data such as soil moisture sensors.

Uncertainties in determination of dilatation gravity mainly arise from the uncertainty of GPS velocities. Calculated horizontal strains have the lowest uncertainty of ~ 0.002 μ strain year⁻¹ over the northwestern Washington State⁴³ thanks to deployment of a dense GPS network. These uncertainties increase to a maximum of ~ 0.018 μ strain year⁻¹ over the northern Vancouver Island and the estimated uncertainty at PGC is ~ 0.011 μ strain year⁻¹. Among the three estimated strains, vertical strain has the highest uncertainty (δE_{zz}) as we only have one surface value for the vertical movement:

$$\delta E_{zz} = \frac{u_z}{H_c} \sqrt{\left(\frac{\delta u_z}{u_z}\right)^2 + \left(\frac{\delta H_c}{H_c}\right)^2}, \quad (6)$$

where H_c and δH_c are the depth of effective strain and its uncertainty, and u_z and δu_z represent the vertical GPS displacement rate and its uncertainty. While the uncertainty in estimation of the depth of effective strain can introduce some uncertainty (10–15 km error in 45 km depth), large uncertainties in vertical velocities dominate the uncertainty in vertical strain (0.02 μ strain year⁻¹ at PGC). Applying the error propagation to calculation of volumetric dilatation results in dilatation uncertainties that range from 0.02 to 0.031 μ strain year⁻¹, where the uncertainty at the PGC reaches to 0.025 μ strain year⁻¹. Propagation of dilatation uncertainty to estimated dilatation gravity via Eqs. (4) and (5) is done by adding the uncertainty contribution of each block which leads to an uncertainty of ~ 0.26 μ Gal year⁻¹ at PGC.

Data availability

The superconducting gravity dataset that supports the findings of this study is available in the Figshare online open access repository at <https://doi.org/10.6084/m9.figshare.20827174>.

Tremor data is available at <https://pnsn.org/tremor>.

GPS data is available at <http://geodesy.unr.edu/index.php>.

GLDAS hydrological data is available at: <https://giovanni.gsfc.nasa.gov/giovanni/>.

Code availability

GMT codes and sample data for creating maps in this study are available at https://figshare.com/articles/software/GMT_codes/20954362. The code for gravity data processing is available at http://igets.u-strasbg.fr/soft_and_tool.php. The code for calculation of strain is available at <https://sourceforge.net/projects/geostrain/>.

Received: 13 January 2022; Accepted: 13 October 2022;

Published online: 05 November 2022

References

1. Tanaka, Y., Heki, K., Matsuo, K. & Shestakov, N. V. Crustal subsidence observed by GRACE after the 2013 Okhotsk deep-focus earthquake. *Geophys. Res. Lett.* **42**, 3204–3209 (2015).
2. Xu, C., Su, X., Liu, T. & Sun, W. Geodetic observations of the co- and post-seismic deformation of the 2013 Okhotsk Sea deep-focus earthquake. *Geophysical Journal International* **209**, 1924–1933 (2017).
3. Sun, W. & Okubo, S. Coseismic deformations detectable by satellite gravity missions: A case study of Alaska (1964, 2002) and Hokkaido (2003) earthquakes in the spectral domain. *J. Geophys. Res.* **109**, B04405 (2004).
4. Heki, K. & Matsuo, K. Coseismic gravity changes of the 2010 earthquake in central Chile from satellite gravimetry. *Geophys. Res. Lett.* **37**, 701–719 (2010).
5. Wang, L., Shum, C. K., Simons, F. J., Tapley, B. & Dai, C. Coseismic and postseismic deformation of the 2011 Tohoku-Oki earthquake constrained by GRACE gravimetry. *Geophys. Res. Lett.* **39**, L07301 (2012).
6. Han, S.-C., Riva, R., Sauber, J. & Okal, E. Source parameter inversion for recent great earthquakes from a decade-long observation of global gravity fields. *J. Geophys. Res. Solid Earth* **118**, 1240–1267 (2013).
7. Liangyu, Z., Qingliang, W. & Yiqing, Z. Theoretical simulation of the effect of deformation on local gravity in a density gradient zone. *Geodesy and Geodynamics* **4**, 9–16 (2013).
8. Eshagh, M., Fatolazadeh, F. & Tenzer, R. Lithospheric stress, strain and displacement changes from GRACE-FO time-variable gravity: case study for Sar-e-Pol Zahab Earthquake 2018. *Geophysical Journal International* **223**, 379–397 (2020).
9. Yin, Z. & Xu, C. Estimating gravity changes caused by crustal strain: application to the Tibetan Plateau. *Geophysical Journal International* **210**, 1191–1205 (2017).
10. Mouyen, M. et al. Expected temporal absolute gravity change across the Taiwanese Orogen, a modeling approach. *Journal of Geodynamics* **48**, 284–291 (2009).
11. Mouyen, M. et al. Investigating possible gravity change rates expected from long-term deep crustal processes in Taiwan. *Geophysical Journal International* **198**, 187–197 (2014).
12. DeMets, C., Gordon, R. G. & Argus, D. F. Geologically current plate motions. *Geophysical Journal International* **181**, 1–80 (2010).
13. Savage, J. C. A dislocation model of strain accumulation and release at a subduction zone. *J. Geophys. Res.* **88**, 4984–4996 (1983).
14. Murray, M. H. & Lisowski, M. Strain accumulation along the Cascadia Subduction Zone. *Geophys. Res. Lett.* **27**, 3631–3634 (2000).
15. Flück, P., Hyndman, R. D. & Wang, K. Three-dimensional dislocation model for great earthquakes of the Cascadia Subduction Zone. *J. Geophys. Res.* **102**, 20539–20550 (1997).
16. Peters, R., Jaffe, B. & Gelfenbaum, G. Distribution and sedimentary characteristics of tsunami deposits along the Cascadia margin of western North America. *Sedimentary Geology* **200**, 372–386 (2007).
17. Peacock, S. M., Christensen, N. I., Bostock, M. G. & Audet, P. High pore pressures and porosity at 35 km depth in the Cascadia subduction zone. *Geology* **39**, 471–474 (2011).

18. Atwater, B. F. et al. The orphan tsunamis of 1700—Japanese clues to a parent earthquake in North America. *Professional Paper* <https://doi.org/10.3133/pp1707> (2005).
19. Hyndman, R. D. & Wang, K. Thermal constraints on the zone of major thrust earthquake failure: the Cascadia Subduction Zone. *J. Geophys. Res.* **98**, 2039–2060 (1993).
20. James, T. S., Clague, J. J., Wang, K. & Hutchinson, I. Postglacial rebound at the northern Cascadia subduction zone. *Quaternary Science Reviews* **19**, 1527–1541 (2000).
21. Burgette, R. J., Weldon, R. J. & Schmidt, D. A. Interseismic uplift rates for western Oregon and along-strike variation in locking on the Cascadia subduction zone. *J. Geophys. Res.* **114**, B01408 (2009).
22. Saffer, D. M. & Tobin, H. J. Hydrogeology and mechanics of Subduction zone forearcs: fluid flow and pore pressure. *Annu. Rev. Earth Planet. Sci.* **39**, 157–186 (2011).
23. Obara, K. Nonvolcanic deep tremor associated with subduction in Southwest Japan. *Science* **296**, 1679–1681 (2002).
24. Dragert, H., Wang, K. & Rogers, G. Geodetic and seismic signatures of episodic tremor and slip in the northern Cascadia subduction zone. *Earth Planet Sp* **56**, 1143–1150 (2004).
25. Nadeau, R. M. & Dolenc, D. Nonvolcanic tremors deep beneath the San Andreas Fault. *Science* **307**, 389–389 (2005).
26. Payero, J. S. et al. Nonvolcanic tremor observed in the Mexican subduction zone. *Geophys. Res. Lett.* **35**, L07305 (2008).
27. Peterson, C. L. & Christensen, D. H. Possible relationship between nonvolcanic tremor and the 1998–2001 slow slip event, south central Alaska. *J. Geophys. Res.* **114**, B06302 (2009).
28. Dragert, H. & Wang, K. Temporal evolution of an episodic tremor and slip event along the northern Cascadia margin. *J. Geophys. Res.* **116**, B12406 (2011).
29. Beroza, G. C. & Ide, S. Slow Earthquakes and Nonvolcanic Tremor. *Annu. Rev. Earth Planet. Sci.* **39**, 271–296 (2011).
30. Duckworth, W. C., Amos, C. B., Schermer, E. R., Loveless, J. P. & Rittenour, T. M. Slip and Strain Accumulation Along the Sadie Creek Fault, Olympic Peninsula, Washington. *J. Geophys. Res. Solid Earth* **126**, (2021).
31. Wech, A. G., Creager, K. C. & Melbourne, T. I. Seismic and geodetic constraints on Cascadia slow slip. *J. Geophys. Res.* **114**, B10316 (2009).
32. Krogstad, R. D., Schmidt, D. A., Weldon, R. J. & Burgette, R. J. Constraints on accumulated strain near the ETS zone along Cascadia. *Earth and Planetary Science Letters* **439**, 109–116 (2016).
33. Miller, M. M. et al. GPS-determination of along-strike variation in Cascadia margin kinematics: Implications for relative plate motion, subduction zone coupling, and permanent deformation. *Tectonics* **20**, 161–176 (2001).
34. Svarc, J. L. Strain accumulation and rotation in western Oregon and southwestern Washington. *J. Geophys. Res.* **107**, 2087 (2002).
35. Lambert, A., Courtier, N. & James, T. S. Long-term monitoring by absolute gravimetry: Tides to postglacial rebound. *Journal of Geodynamics* **41**, 307–317 (2006).
36. Mazzotti, S., Lambert, A., Courtier, N., Nikolaishen, L. & Dragert, H. Crustal uplift and sea level rise in northern Cascadia from GPS, absolute gravity, and tide gauge data. *Geophys. Res. Lett.* **34**, L15306 (2007).
37. Mazzotti, S., Lambert, A., Henton, J., James, T. S. & Courtier, N. Absolute gravity calibration of GPS velocities and glacial isostatic adjustment in mid-continent North America. *Geophys. Res. Lett.* **38**, L24311 (2011).
38. Warburton, R. J., Pillai, H. & Reineman, R. C. Initial Results with the New GWR iGrav™ Superconducting Gravity Meter. in *Proc. IAG Symp. on Terrestrial Gravimetry: Static and Mobile Measurements (TG-SMM2010), 22–25 June 2010, Russia, Saint Petersburg*, 138 (2010).
39. Kao, R., Kabirzadeh, H., Kim, J. W., Neumeier, J. & Sideris, M. G. Detecting small gravity change in field measurement: simulations and experiments of the superconducting gravimeter—iGrav. *J. Geophys. Eng.* **11**, 045004 (2014).
40. Kim, J. W., Neumeier, J., Kao, R. & Kabirzadeh, H. Mass balance monitoring of geological CO₂ storage with a superconducting gravimeter — A case study. *Journal of Applied Geophysics* **114**, 244–250 (2015).
41. Blewitt, G., Kreemer, C., Hammond, W. C. & Gazeaux, J. MIDAS robust trend estimator for accurate GPS station velocities without step detection. *J. Geophys. Res. Solid Earth* **121**, 2054–2068 (2016).
42. Blewitt, G., Hammond, W. & Kreemer, C. Harnessing the GPS Data Explosion for Interdisciplinary Science. *Eos* **99**, 19–22 (2018).
43. Goudarzi, M. A., Cocard, M. & Santerre, R. GeoStrain: An open source software for calculating crustal strain rates. *Computers & Geosciences* **82**, 1–12 (2015).
44. McCaffrey, R., King, R. W., Payne, S. J. & Lancaster, M. Active tectonics of northwestern U.S. inferred from GPS-derived surface velocities. *J. Geophys. Res. Solid Earth* **118**, 709–723 (2013).
45. McCaffrey, R. et al. Fault locking, block rotation and crustal deformation in the Pacific Northwest. *Geophysical Journal International* **169**, 1315–1340 (2007).
46. Cruikshank, K. M. & Peterson, C. D. Late stage interseismic strain interval, Cascadia Subduction Zone. *Margin, USA and Canada. OJER* **06**, 1–34 (2017).
47. Calvert, A. J., Bostock, M. G., Savard, G. & Unsworth, M. J. Cascadia low frequency earthquakes at the base of an overpressured subduction shear zone. *Nat Commun* **11**, 3874 (2020).
48. Tichelaar, B. W. & Ruff, L. J. Depth of seismic coupling along subduction zones. *J. Geophys. Res.* **98**, 2017–2037 (1993).
49. Crosson, R. S. & Owens, T. J. Slab geometry of the Cascadia Subduction Zone beneath Washington from earthquake hypocenters and teleseismic converted waves. *Geophys. Res. Lett.* **14**, 824–827 (1987).
50. Khazaradze, G., Qamar, A. & Dragert, H. Tectonic deformation in western Washington from continuous GPS measurements. *Geophys. Res. Lett.* **26**, 3153–3156 (1999).
51. Piretzidis, D., Sra, G., Karantaidis, G., Sideris, M. G. & Kabirzadeh, H. Identifying presence of correlated errors using machine learning algorithms for the selective de-correlation of GRACE harmonic coefficients. *Geophysical Journal International* **215**, 375–388 (2018).
52. Meurers, B. Superconducting Gravimeter Calibration by CoLocated Gravity Observations: Results from GWR C025. *International Journal of Geophysics* **2012**, 1–12 (2012).
53. Wenzel, H. G. The nanogal software: earth tide data processing package ETERNA 3.30. in *Marees Terrestres Bulletin d'Informations* **124**, 9425–9439 (1996). vol.
54. Seitz, F., Stuck, J. & Thomas, M. Consistent atmospheric and oceanic excitation of the Earth's free polar motion. *Geophysical Journal International* **157**, 25–35 (2004).
55. Warburton, R. J. & Goodkind, J. M. The influence of barometric-pressure variations on gravity. *Geophysical Journal International* **48**, 281–292 (1977).
56. Abd El-Gelil, M., Pagiatakis, S. & El-Rabbany, A. Frequency-dependent atmospheric pressure admittance of superconducting gravimeter records using least squares response method. *Physics of the Earth and Planetary Interiors* **170**, 24–33 (2008).
57. Rodell, M. et al. The Global Land Data Assimilation System. *Bull. Amer. Meteor. Soc.* **85**, 381–394 (2004).
58. Meurers, B., Van Camp, M. & Petermans, T. Correcting superconducting gravity time-series using rainfall modelling at the Vienna and Membach stations and application to Earth tide analysis. *J. Geod* **81**, 703–712 (2007).
59. Bower, D. R. & Courtier, N. Precipitation effects on gravity measurements at the Canadian Absolute Gravity Site. *Physics of the Earth and Planetary Interiors* **106**, 353–369 (1998).
60. De Linage, C., Hinderer, J. & Rogister, Y. A search for the ratio between gravity variation and vertical displacement due to a surface load: Ratio between gravity variation and vertical displacement due to a surface load. *Geophysical Journal International* **171**, 986–994 (2007).
61. Heki, K. & Arief, S. Crustal response to heavy rains in Southwest Japan 2017–2020. *Earth and Planetary Science Letters* **578**, 117325 (2022).
62. Boy, J.-P. & Hinderer, J. Study of the seasonal gravity signal in superconducting gravimeter data. *Journal of Geodynamics* **41**, 227–233 (2006).
63. Han, S.-C., Shum, C. K., Bevis, M., Ji, C. & Kuo, C.-Y. Crustal Dilatation Observed by GRACE After the 2004 Sumatra-Andaman Earthquake. *Science* **313**, 658–662 (2006).
64. Cambiotti, G., Burdoni, A., Sabadini, R. & Colli, L. GRACE gravity data help constraining seismic models of the 2004 Sumatran earthquake. *J. Geophys. Res.* **116**, B10403 (2011).
65. Plouff, D. Gravity and magnetic fields of polygonal prisms and application to magnetic terrain corrections. *GEOPHYSICS* **41**, 727–741 (1976).
66. Kabirzadeh, H., Kim, J. W. & Sideris, M. G. Micro-gravimetric monitoring of geological CO₂ reservoirs. *International Journal of Greenhouse Gas Control* **56**, 187–193 (2017).
67. Kabirzadeh, H., Kim, J. W., Sideris, M. G., Vatankhah, S. & Kwon, Y. K. Coupled inverse modelling of tight CO₂ reservoirs using gravity and ground deformation data. *Geophysical Journal International* **216**, 274–286 (2019).
68. Kabirzadeh, H., Kim, J. W., Sideris, M. G. & Vatankhah, S. Analysis of surface gravity and ground deformation responses of geological CO₂ reservoirs to variations in CO₂ mass and density and reservoir depth and size. *Environ Earth Sci* **79**, 163 (2020).
69. Kabirzadeh, H., Ali, M. Y., Lee, G. H. & Kim, J. W. Determining Infracambrian Hormuz Salt and Basement Structures Offshore Abu Dhabi by Joint Analysis of Gravity and Magnetic Anomalies. *SPE Reservoir Evaluation & Engineering* **24**, 238–249 (2021).
70. Crossley, D., de Linage, C., Hinderer, J., Boy, J.-P. & Famiglietti, J. A comparison of the gravity field over Central Europe from superconducting gravimeters, GRACE and global hydrological models, using EOF analysis:

Ground-satellite gravity comparisons in Europe. *Geophysical Journal International* **189**, 877–897 (2012).

71. Wessel, P. & Smith, W. H. F. New, improved version of generic mapping tools released. *Eos Trans. AGU* **79**, 579–579 (1998).
72. McCrory, P. A., Blair, J. L., Oppenheimer, D. H. & Walter, S. R. *Depth to the Juan de Fuca slab beneath the Cascadia subduction margin— A 3-D model for sorting earthquakes*. *Data Series* <https://pubs.er.usgs.gov/publication/ds91> <https://doi.org/10.3133/ds91> (2004).

Acknowledgements

We thank Dr. Juergen Neumeyer for his support and advice. Discovery Grants of Natural Sciences and Engineering Research Council of Canada (NSERC) (Grant #RGPIN-2019-07190) and Brain Pool Program of Ministry of Science and ICT (MSIT) through the Research Foundation of Korea (Project #2020H1D3A2A01085842) awarded to J.W.K. supported elements of this research. Generic Mapping Tools (GMT) was used to generate some of the figures in this publication.

Author contributions

H.K. contributed to the conceptualization of the research project, the development of methodology, the data collection and processing, the visualization and writing of the original draft, along with review and editing of revisions. J.W.K. is the project leader and contributed to the writing and revising of the manuscript. A.H.N. contributed to the collecting and processing of GPS and Tremor data and the preparation of the manuscript. J.H. contributed to the gravity data collection and processing, along with review and editing of revisions. R.K. contributed to the data collection and processing, the visualization and writing of the original draft, along with review and editing of revisions. M.G.S. contributed to the commenting of the results and revising of the manuscript.

Competing interests

The authors declare no competing interests.

Additional information

Supplementary information The online version contains supplementary material available at <https://doi.org/10.1038/s43247-022-00586-4>.

Correspondence and requests for materials should be addressed to Hojjat Kabirzadeh.

Peer review information *Communications Earth & Environment* thanks the anonymous reviewers for their contribution to the peer review of this work. Primary Handling Editors: Teng Wang, Joe Aslin. Peer reviewer reports are available.

Reprints and permission information is available at <http://www.nature.com/reprints>

Publisher's note Springer Nature remains neutral with regard to jurisdictional claims in published maps and institutional affiliations.



Open Access This article is licensed under a Creative Commons Attribution 4.0 International License, which permits use, sharing, adaptation, distribution and reproduction in any medium or format, as long as you give appropriate credit to the original author(s) and the source, provide a link to the Creative Commons license, and indicate if changes were made. The images or other third party material in this article are included in the article's Creative Commons license, unless indicated otherwise in a credit line to the material. If material is not included in the article's Creative Commons license and your intended use is not permitted by statutory regulation or exceeds the permitted use, you will need to obtain permission directly from the copyright holder. To view a copy of this license, visit <http://creativecommons.org/licenses/by/4.0/>.

© The Author(s) 2022